




Article

Modified BaMnO₃-Based Catalysts for Gasoline Particle Filters (GPF): A Preliminary Study

Verónica Torregrosa-Rivero ^{*}, María-Salvadora Sánchez-Adsuar  and María-José Illán-Gómez 

Carbon Materials and Environment Research Group, Department of Inorganic Chemistry, Faculty of Science, University of Alicante San Vicente del Raspeig, 03690 Alicante, Spain

* Correspondence: vero.torregrosa@ua.es

Abstract: Gasoline engines, mainly gasoline direct injection engines (GDI) require, in addition to three-way catalysts (TWC), a new catalytic system to remove the formed soot. Gasoline Particle Filters (GPF) are, among others, a possible solution. BaMnO₃ and copper-doped BaMnO₃ perovskites seem to be a feasible alternative to current catalysts for GPF. The physical and chemical properties of these two perovskites determining the catalytic performance have been modified using different synthesis routes: (i) sol-gel, (ii) modified sol-gel and (iii) hydrothermal. The deep characterization allows concluding that: (i) all samples present a perovskite-like structure (hexagonal), except BMC3 which shows a polytype one (due to the distortion caused by copper insertion in the lattice), and (ii) when a low calcination temperature is used during synthesis, the sintering effect decreases and the textural properties, the reducibility and the oxygen mobility are improved. The study of soot oxidation simulating the hardest GDI scenarios reveals that, as for diesel soot removal, the best catalytic performance involves the presence of oxygen vacancies to adsorb and activate oxygen and a labile Mn (IV)/Mn (III) redox pair to dissociate the adsorbed oxygen. The combination of both properties allows the transport of the dissociated oxygen towards the soot.

Keywords: perovskite; carbon black; GPF; soot oxidation



Citation: Torregrosa-Rivero, V.; Sánchez-Adsuar, M.-S.; Illán-Gómez, M.-J. Modified BaMnO₃-Based Catalysts for Gasoline Particle Filters (GPF): A Preliminary Study. *Catalysts* **2022**, *12*, 1325. <https://doi.org/10.3390/catal12111325>

Academic Editor: Hamidreza Arandiyan

Received: 30 September 2022

Accepted: 25 October 2022

Published: 28 October 2022

Publisher's Note: MDPI stays neutral with regard to jurisdictional claims in published maps and institutional affiliations.



Copyright: © 2022 by the authors. Licensee MDPI, Basel, Switzerland. This article is an open access article distributed under the terms and conditions of the Creative Commons Attribution (CC BY) license (<https://creativecommons.org/licenses/by/4.0/>).

1. Introduction

Currently, perovskite oxides (ABO₃) are being studied as a promising alternative to PGM-based catalysts for automotive exhaust abatement, due to their high thermal stability, low cost and tunable redox properties mainly achieved by the control of the composition [1–7]. In several studies focused on developing new strategies to improve the physical, chemical, and catalytic properties of these solids, the following variables are analyzed:

- * The combination of different A and B cations, since almost the 90% of the elements can be stabilized in a mixed oxide with perovskite-like structure [8,9].
- * The partial substitution of A and/or B cations, which allows achieving non-usual oxidation states for the B cation and/or generating oxide ion vacancies [10–13].
- * The use of perovskite as substrates [1,14–17] or supporting the perovskite [18–24].
- * The increase in the surface area by using different synthesis methods: solid-state, sol-gel, reactive grinding and hydrothermal, among others [15,25–32].

It is well-known that manganites (AMnO₃) are useful for oxidation applications because of their redox properties due to the electronic configuration of manganese, with oxidation states of (III) and (IV) [11]. Moreover, Mn (III) is affected by the Jahn–Teller effect, a distortion to remove the degeneration due to asymmetrically filled d orbitals achieving lower energy states and modifying the crystal structure [33–35], but also generates some structural defects [11]. The coexistence of both oxidation states, especially an enriched Mn (IV) surface, improves the oxygen mobility, enhancing the catalytic activity for soot oxidation [36]. It is also remarkable that manganese is abundant, and then, low cost. On the other hand, copper-doped perovskites, such as LaCo_{1–x}Cu_xO₃ [2], LaFe_{1–x}Cu_xO₃ [3],

LaNi_{0.5}Cu_{0.5}O₃ [4] or LaMn_{1-x}Cu_xO₃ [29,37], have shown promising results for catalytic oxidation processes. In fact, a remarkable synergistic effect between copper and manganese has been observed for these solids, which boosts the reducibility of both cations and allows the synthesis of bifunctional catalysts [29].

It has been widely proved that soot oxidation can be catalyzed by O₂, by NO and by a mixture of both NO-O₂ [27,38–40]. Nevertheless, the composition of a GDI exhaust is poor in NO_x, with the fuel cuts (i.e., when the engine pumps air from the intake to the exhaust [41,42]) being the only source of oxygen, and most of this is used by the three-way catalyst (TWC). Therefore, a good catalyst for this application should be active to adsorb oxygen during the fuel cuts mode and release it in regular operating conditions. T. Boger et al. proved that the passive oxidation of soot could be performed at the high-temperature exhaust of GDI engines (400–700 °C) [41]; thus, the soot oxidation process occurs through different mechanisms as a function of the composition and temperature. Currently, GDI engines present a high fuel economy and reduced CO₂ emission (compared to other gasoline engines), which positioned them as the most bought passenger car in 2017 [43]. However, due to the presence of a fuel-rich stage, leading to the incomplete combustion of the remaining fuel into the chamber, a large amount of small soot particles are formed that present a high health risk [42,43].

Perovskite-based catalysts could show a great oxygen storage capacity since O₂ can be adsorbed in the oxygen vacancies [38]. Because of that, in this paper, the BaMnO₃ solids have been used for soot oxidation under two different atmospheres: in an inert atmosphere (He), simulating the regular operation conditions of a GDI engine; and in a slight oxidant atmosphere (1% O₂/He), which reproduces severe fuel cut operation conditions, but also it is the typical O₂ concentration at the turbine-GDI engine exit, i.e., upstream of the TWC [44].

In previous studies, BaMnO₃ and BaMn_{1-x}Cu_xO₃ mixed oxides with a perovskite-like structure, obtained by different synthesis procedures that provide specific chemical and physical properties, have shown interesting catalytic activity for NO to NO₂ oxidation and for NO_x-assisted soot oxidation [45–47]. In this work, these samples are tested as feasible catalysts for GPF systems. To improve the chemical and physical properties of the BaMnO₃ catalyst, two approaches have been employed: (i) partial substitution of manganese by copper, obtaining solids with BaMn_{1-x}Cu_xO₃ composition in which $x = 0, 0.1, 0.2,$ and 0.3 that are prepared by conventional sol-gel synthesis [45]; (ii) synthesis of BaMnO₃ samples by modified sol-gel by using carbon black as a pore-forming material and three calcination temperatures (600 °C, 700 °C and 850 °C, the last one being equal to that used in conventional sol-gel synthesis) [46]; and by hydrothermal synthesis followed by a calcination step at 600 °C.

2. Results and Discussion

2.1. Characterization

The fresh catalysts were deeply characterized, the results being thoroughly discussed in previous published articles by the authors [45–47]. Therefore, in this section, a comparison of the most relevant properties of catalysts has been presented in order to correlate the chemical and physical properties to the catalytic performance for soot oxidation under GDI conditions. Table 1 gathers the main information about the composition synthesis procedure details (as calcination temperature) and the most relevant properties for each sample.

2.1.1. Copper Content (ICP-OES) and Textural Properties

Table 1 shows the nominal and experimental (obtained by ICP-OES analysis) copper content and the BET surface area of the BaMn_{1-x}Cu_xO₃ series and BaMnO₃ catalysts obtained through different synthesis routes. The results reveal that the sol-gel procedure allowed the incorporation of the required copper amount for each catalyst, because the actual value was closer to the nominal one. On the other hand, as ceramic solids with poorly developed porosity [48–50], the BaMnO₃ solids presented a Type IV isotherm (not shown) and low BET specific surface area. However, the synthesis procedure seemed to

slightly modify the porosity, and the use of carbon black as pore-forming material allowed a slight increase in the BET surface value for BM-C600 and BM-C700. This is due to the lower calcination temperature used during their synthesis which decreased the sintering effects. On the contrary, the use of the hydrothermal method seemed to not affect the porosity development, because the BET surface area of BM-H was similar to that observed for BM.

Table 1. Chemical composition, copper content by ICP-OES and BET surface area of the catalysts.

Catalyst	Composition	Synthesis Procedure	T _{cal} (°C)	Nominal Cu (wt%)	Cu-ICP-OES (wt%)	S _{BET} (m ² ·g ⁻¹)
BM	BaMnO ₃			-	-	5
BMC1	BaMn _{0.9} Cu _{0.1} O ₃	Conventional	850	2.6	2.4	4
BMC2	BaMn _{0.8} Cu _{0.2} O ₃	Sol-gel		4.8	4	
BMC3	BaMn _{0.7} Cu _{0.3} O ₃			7.6	4	
BM-C600	BaMnO ₃	Modified sol-gel	600	-	-	20
BM-C700	BaMnO ₃		700	-	-	21
BM-C850	BaMnO ₃		850	-	-	7
BM-H	Ba _{0.9} MnO ₃	Hydrothermal	600	-	-	10

2.1.2. Crystal Structure: XRD

The X-ray patterns, presented in Figure 1, show that both synthesis methods allowed the formation of a BaMnO₃ perovskite-like structure as the main crystal phase. However, depending on the synthesis method and the copper amount, different minority phases were detected.

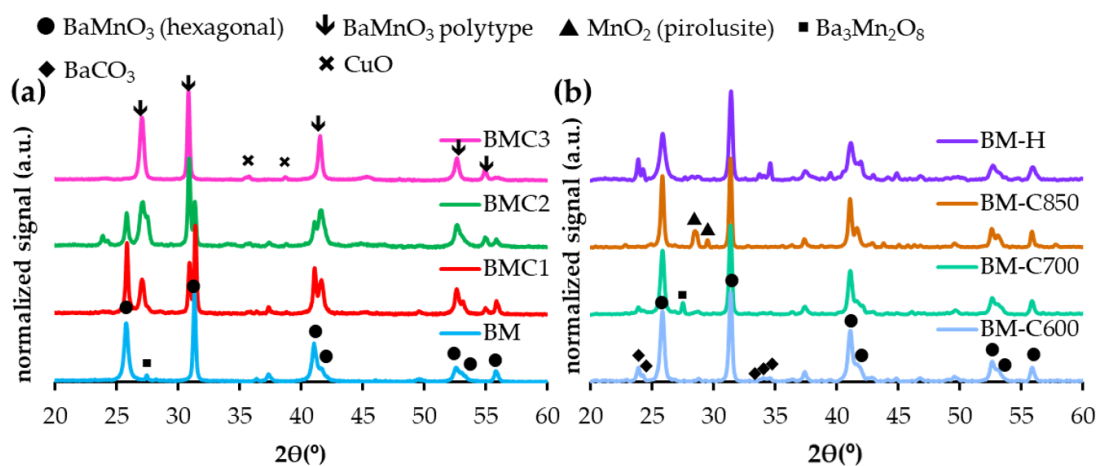


Figure 1. X-ray patterns of (a) BaMn_{1-x}Cu_xO₃ series and (b) BaMnO₃ catalysts.

For the perovskites obtained through conventional sol-gel synthesis, the crystal phases detected depended on the amount of copper. BM, the sample without copper, presented as the main crystal phase the BaMnO₃ hexagonal (PDF number: 026-0168), and for the BaMn_{1-x}Cu_xO₃ series, as the copper content increased, the hexagonal phase decreased in favor of the polytype crystal phase. This phase was formed because the insertion of copper into the perovskite lattice generated a distortion in the original hexagonal structure. For BMC3, the catalyst with the highest amount of copper, the BaMnO₃ polytype phase, was the only perovskite structure, and low intense peaks of CuO were observed. The distortion of the structure was also observed in the lattice parameters, calculated for both perovskite phases, and is shown in Table 2.

All the catalysts obtained through the modified sol-gel synthesis showed the BaMnO₃ hexagonal structure as the main crystal phase, and the calcination temperature determined the composition of the minority phases. BM-C600 presented some barium carbonate due to

the low calcination temperature (600 °C) and, as the calcination temperature increased, the presence of barium carbonate decreased up to BM-C850, for which this crystal phase was not detected at all.

Table 2. Crystal phase, average crystal size and lattice parameters of the catalysts.

Catalyst	Identified Crystal Phases (XRD)	Average Crystal Size (nm) ^a	Lattice Parameters ^b	
			a (nm)	c (nm)
BM	BaMnO ₃ hexagonal Ba ₃ Mn ₂ O ₈	40	5.703	4.831
BMC1	BaMnO ₃ hexagonal BaMnO ₃ polytype	39 (38)	5.698 (5.774)	4.808 (4.364)
BMC2	BaMnO ₃ polytype BaMnO ₃ hexagonal, CuO	43 (36)	5.695 (5.784)	4.811 (4.365)
BMC3	BaMnO ₃ polytype, CuO	(33)	(5.792)	(4.368)
BM-C600	BaMnO ₃ hexagonal Ba ₃ Mn ₂ O ₈ BaCO ₃	27	5.693	4.803
BM-C700	BaMnO ₃ hexagonal Ba ₃ Mn ₂ O ₈ BaCO ₃	31	5.693	4.798
BM-C850	BaMnO ₃ hexagonal Ba ₃ Mn ₂ O ₈ BaCO ₃	33	5.693	4.805

^a by Scherrer equation using the main diffraction peak of BaMnO₃ hexagonal ($\approx 31.4^\circ$); in brackets are the crystallographic data calculated for the BaMnO₃ polytype phase (main diffraction peak $\approx 30.9^\circ$)^b from the main diffraction peaks of the BaMnO₃ hexagonal $\approx 31.4^\circ$ (110) and $\approx 25.8^\circ$ (101); in brackets are the crystallographic data calculated for the BaMnO₃ polytype phase (main diffraction peaks $\approx 30.9^\circ$ (110) and $\approx 27.0^\circ$ (101)).

For the samples prepared using hydrothermal synthesis (BM-H), the presence of some barium carbonate was also detected due to the low temperature used during the synthesis process. Moreover, the lattice parameter values for this sample indicated a modification of the BaMnO₃ hexagonal structure that could be related to the higher amount of Mn (IV) present in the perovskite structure of BM-H, which is formed to compensate for the positive charge imbalance due to its barium deficiency [51,52].

The average crystal size, calculated by the Scherrer equation and gathered in Table 2, showed the expected trend with the calcination temperature: it decreased with the calcination temperature. Therefore, BM-C600 showed the lowest average crystal size, with the highest values being observed for the samples calcined at 850 °C.

2.1.3. Surface Composition

In Figure 2, the spectra corresponding to the Mn 2p^{3/2}, O 1s and Cu 3p^{3/2} transitions of catalysts are shown. Briefly, Figure 2a,b reveal the coexistence of two oxidation states of manganese: Mn (III), due to the signal over 645 eV assigned to a satellite peak of Mn (III), and the signal at c.a. 643 eV [53,54] corresponding to Mn (IV). The Mn (IV)/Mn (III) ratio, shown in Figure 3a, points out Mn (III) as the main oxidation state on the surface for all catalysts, since all of them are lower than 1. For the BaMn_{1-x}Cu_xO₃ series, the copper inserted into the perovskite lattice (which promotes the polytype phase) led to an increase in the amount of Mn (III); therefore, the electroneutrality must be achieved by the generation of oxygen vacancies. On the other hand, for the BM-CX samples, the amount of Mn (IV) increased with the calcination temperature, and also, some oxygen vacancies should be present on the surface to compensate for the deficit of positive charge due to the presence of Mn (III). For BM-H, a Mn (IV)/Mn (III) ratio higher than for BM was detected, as the positive charge imbalance due to the barium deficiency has to be compensated [51,52]; so, the ratio was close to 1, meaning that the amount of both oxidation states on the surface was almost the same.

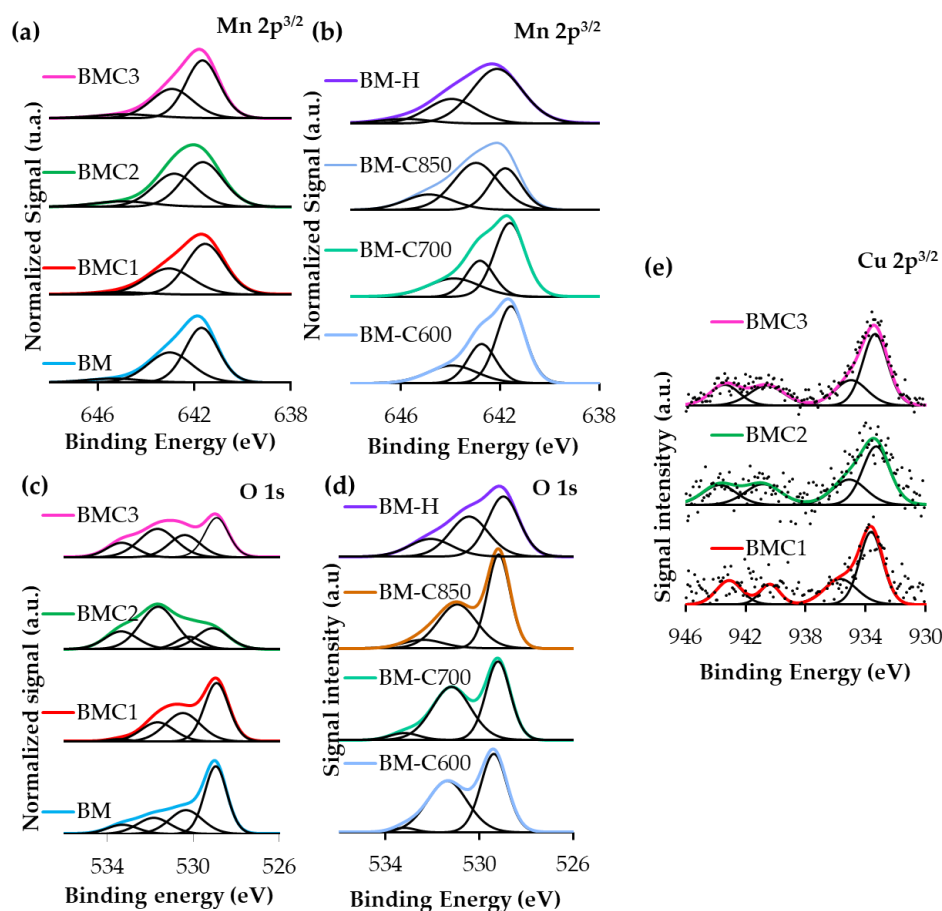


Figure 2. XPS transition spectra of $Mn2p^{3/2}$ (a,b), $O1s$ (c,d) and $Cu2p^{3/2}$ (e) for $BaMn_{1-x}Cu_xO_3$ and $BaMnO_3$ catalyst series.

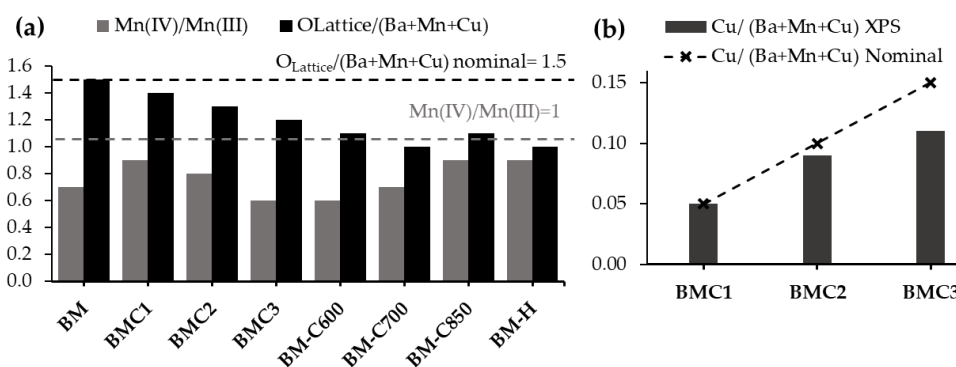


Figure 3. XPS ratios (a) $Mn(IV)/Mn(III)$ and $O_{Lattice}/(Ba + Mn + Cu)$ and (b) $Cu/(Ba + Mn + Cu)$ for the $BaMn_{1-x}Cu_xO_3$ and $BaMnO_3$ catalyst series.

Figure 2c,d compare the XPS spectra corresponding to the $O1s$ transition, showing three different contributions assigned to lattice oxygen ($O_{Lattice}$, ca. 529 eV), oxygen from the surface groups (ca. 531 eV), and oxygen from moisture (ca. 533 eV) [55–57]. In these spectra, it is clearly observable that copper introduction promoted the generation of surface oxygen species, such as adsorbed surface oxygen and hydroxyl/carbonate species (corresponding to moisture), as the area corresponding to these species increased from BM to the BMC3 catalyst. Therefore, it seems that to compensate for the deficit of positive charge due to copper and to achieve the electroneutrality, a lower amount of oxygen exits on the surface.

In Figure 3a, the values of the $O_{Lattice}/(Ba + Mn + Cu)$ ratio for all the catalysts are gathered. It reveals the presence of oxygen vacancies because the values are lower than

the nominal one (1.5) [58] for the BM-CX series and for the copper-containing catalysts. The generation of oxygen vacancies is a mechanism to compensate for the positive charge defect due to the presence of Mn (III), Mn (III) and Cu (II) for copper-containing samples, and barium deficit for BM-H. Therefore, as was expected, as the copper amount increased, the $O_{\text{Lattice}}/(\text{Ba} + \text{Mn} + \text{Cu})$ ratio decreased. It was observed that the modified sol-gel and hydrothermal synthesis allowed an increase in the oxygen vacancies on the surface since the ratio was lower than for BM. The calcination temperature for the BM-CX samples did not play a significant role since no significant differences were observed.

Figure 2e shows the $\text{Cu}2p^{3/2}$ transition spectra of the samples, in which the position of the main band over 933 eV and the shake-up satellite peaks (at c.a. 940 eV and 944 eV) indicate the presence of Cu (II) [2,17,31,59]. In general, all the catalysts show a similar $\text{Cu}2p^{3/2}$ spectrum, in which two different contributions, corresponding to two degrees of copper interaction with the perovskite, are suggested: (i) the signal over 935 eV could be assigned to copper with a strong electronic interaction with the perovskite, and (ii) the signal at c.a. 933.5 eV could correspond to copper with a weak electron interaction with the perovskite [59,60]. The $\text{Cu}/(\text{Ba} + \text{Mn} + \text{Cu})$ ratio provides information about the distribution of copper over the perovskite surface. In Figure 3b, the ratios are compared to the nominal value and it seems that copper was inserted into the perovskite lattice only for BMC3, as concluded from the XRD data. Therefore, copper was homogeneously distributed on the perovskite for BMC1 and BMC2, since these two copper-containing samples showed surface ratios close to the nominal one (cross on Figure 3b).

2.1.4. Reducibility: H_2 -TPR

The hydrogen consumption profiles, shown in Figure 4, revealed the presence of two manganese species with different oxidation states in all the BaMnO_3 samples, as has been also observed on the surface using XPS. The profiles can be divided into three regions, in which different reduction processes occur.

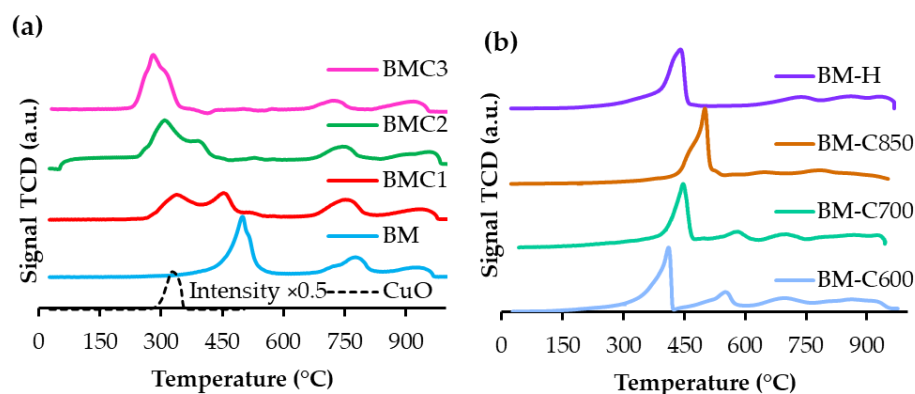


Figure 4. Hydrogen consumption profiles in TPR conditions of (a) $\text{BaMn}_{1-x}\text{Cu}_x\text{O}_3$ series and (b) BaMnO_3 catalysts.

The hydrogen consumption between 200 °C and 600 °C was due to the reduction of manganese species. The asymmetry of the peak reveals that the reduction of manganese was carried out in two steps, pointing out the presence of Mn (IV), which was reduced at a lower temperature. The reduction of Mn (IV) to Mn (III) was detected as a shoulder of the main peak corresponding to Mn (III) reduction to Mn (II), including the initial Mn (III) present and that formed by Mn (IV) reduction [35,61].

For the $\text{BaMn}_{1-x}\text{Cu}_x\text{O}_3$ series (Figure 4a), it can be concluded that copper incorporation promoted the reduction of manganese since the reduction temperature of Mn (IV)/Mn (III) was shifted to lower temperatures as the copper content increased. For BMC3, the reduction of Cu (II) and Mn (IV)/Mn (III) was overlapped; therefore, a synergetic effect between copper and manganese should be taking place.

In Figure 4b, the profiles of the samples obtained using the modified sol-gel and the hydrothermal method reveal that the catalysts calcined at lower temperatures (BM-C600, BM-C700 and BM-H) show an improved reducibility since the reduction occurred at a lower temperature than in the BM catalyst. This fact has also been observed by S. Irusta et al. for lanthanum manganites [62] and by Y. Gao et al. for barium manganite [20,63], obtained through conventional sol-gel synthesis and calcined at different temperatures. The H₂-TPR data point out that BM-C600, BM-C700 and BM-H catalysts should present more available surface for the interaction with the gas phase, since surface species are more reducible than bulk species.

It should be noted that, only for the BM-CX series, a hydrogen consumption peak at c.a. 550 °C was observed, which could be due to the presence of the remaining carbon black used as hard template, as has been detected through TGA [46].

At the highest temperature range, the hydrogen consumption around 750 °C was assigned to the decomposition of surface species, while, up to 750 °C, the reduction of Mn (III) bulk to Mn (II) took place. This process was mainly observed in the BM profile as it presented the largest crystal size and, therefore, the lowest amount of boundary manganese [62].

2.1.5. O₂ Desorption: O₂-TPD

The evolved oxygen profiles, shown in Figure 5a,b, reveal that the BaMnO₃ catalysts mainly evolve high-temperature oxygen, called β-O₂, which comes from the BaMnO₃ perovskite lattice, being related to the reduction of Mn (IV) to Mn (III) [64–66] and boosted by the presence of lattice oxygen vacancies. Thus, the O₂-TPD data inform about the oxygen mobility through the lattice [66,67]. The total amount of emitted β-O₂, calculated using the area under the peaks between 700 °C and 950 °C, is included in Figure 5c.

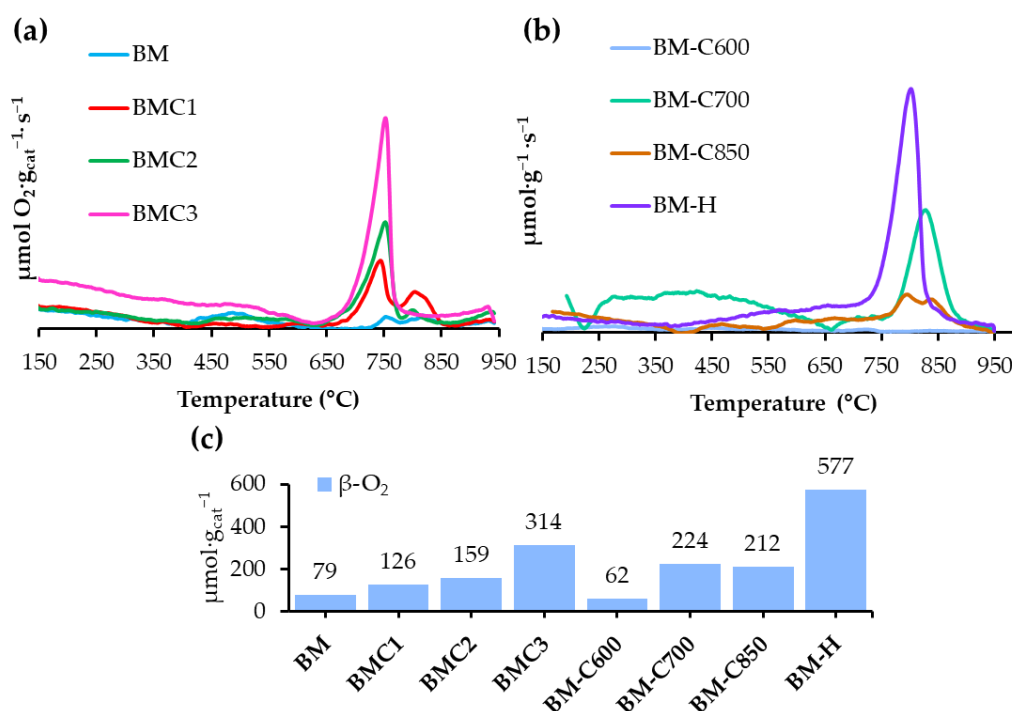


Figure 5. O₂-TPD profiles for (a) BaMn_{1-x}Cu_xO₃ catalysts serie, (b) BaMnO₃ catalysts serie and (c) amount of β-O₂ emitted during O₂-TPD experiments.

The oxygen emission profiles revealed a clear effect of the copper amount, of the calcination temperature, and of the synthesis method. It was observed that the β-O₂ emission was higher as the copper amount increased, suggesting that the amount of copper boosted the oxygen mobility through the ratio of the perovskite lattice, and hence, the manganese

reducibility was also improved (as was concluded from the H₂-TPR experiments). The hydrothermal synthesis allowed the formation of a BaMnO₃ perovskite-like solid (BM-H) with enhanced oxygen mobility, probably due to the higher Mn (IV)/Mn (III) ratio on the surface by XPS (see Figure 3a), and by H₂-TPR for the bulk, and the presence of a high amount of surface oxygen vacancies, promoted by its barium deficiency. However, for the BM-CX series, only BM-C700 and BM-C850 showed a significantly higher emission of β-O₂ than that observed for BM. Note that the BM-C700 sample also evolved oxygen at a low and medium temperature, called α (corresponding to the desorption of oxygen adsorbed on the surface) and α'-O₂ (corresponding to the desorption of oxygen adsorbed on the vacancies), respectively.

In summary, the incorporation of copper and the use of modified sol-gel and hydrothermal synthesis methods yield perovskites, in which Mn (III) and Mn (IV) oxidation states coexist (Mn (III) being the main oxidation state in most of them) and a higher amount of oxygen vacancies on the surface than BM. BMC3 (with the highest amount of copper), BM-C700 and BM-H present an improved reducibility and, hence, a higher oxygen mobility than BM perovskite, which plays an important role in catalyzing oxidation reactions.

2.2. Activity Tests

In previous studies, we found that the combination of a high amount of oxygen defects, a balanced Mn (IV)/Mn (III) ratio, and the presence of surface copper provide high activity for NO and NO₂-assisted soot oxidation processes. In this work, the synthesized samples have been tested as catalysts for soot oxidation under simulated GDI exhaust conditions.

2.2.1. Preliminary Phase: TG-MS Experimental System

The preliminary study for soot oxidation in GDI conditions has been performed in a TG-MS system, which allows the use of low amounts of soot and low gas flow to avoid external mass transfer limitations [68]. In order to simulate the hardest scenario, the soot oxidation tests were carried out under inert atmosphere (0% O₂/He), where the available oxygen only came from the perovskite, and under a slightly oxidant atmosphere (1% O₂/He) which was achieved during fuel cuts [40].

The CO and CO₂ emission profiles during both reaction atmospheres (0% and 1% O₂) are presented in Figure 6. These profiles are expressed as μmol of CO or CO₂ per gram of catalyst and initial soot; therefore, although the bare soot was also tested (see Figure A1 in Appendix A), the corresponding profiles were not included. However, the soot conversion and CO₂ selectivity are included in Figure 7, which gathers the selectivity to CO₂, based on the 44 *m/z* and 28 *m/z* MS signals registered during the soot oxidation experiments, and the percentage of removed soot, which was calculated from the weight loss during the TGA experiment in synthetic air carried out after the catalytic test. As some samples presented barium carbonates (due to the low calcination temperature used during synthesis), an additional experiment was carried out in the absence of soot (see Figure A2 in Appendix A) and the CO and CO₂ emissions were used to correct the values for each catalyst.

Figure 6a,b shows the CO (dotted lines) and CO₂ (solid line) emissions in 1% O₂/He and He atmosphere, respectively, for the BaMn_{1-x}Cu_xO₃ series. The results in 1% O₂/He reveal that all the catalysts were active to catalyze the oxidation of soot to CO₂ because the reaction started at ca. 450 °C, the maximum being located at ca. 700 °C. However, as the amount of copper increased, the catalytic behavior worsened. This could be related to an increase in the amount of Mn (III) (supported by XPS data in Figure 3a) which seems to be less active than Mn (IV) [69]. Similar results have been observed for BaFe_{1-x}Cu_xO₃ catalysts [70,71]. Moreover, as is expected for manganese-based catalysts, independently of the copper amount, all the samples presented a high CO₂ selectivity, being higher than 90%.

On the contrary, in the absence of oxygen, the catalysts were active at temperatures higher than 700 °C because the unique oxygen for soot oxidation came from the perovskite lattice (β-O₂), which seemed to be able to catalyze the soot oxidation, as was also reported for BaFe_{1-x}Cu_xO₃ catalysts [71]. In the conditions used, almost all the soot was removed in

the absence of the catalyst, but the CO₂ selectivity was quite low, whereas in presence of the BaMn_{1-x}Cu_xO₃ catalysts, the selectivity to CO₂ increased as the copper amount increased. The CO and CO₂ profiles (Figure 6b,d) followed the thermodynamically expected product distribution according to the Ellingham diagram, showing a strong correlation between the CO₂ formation and the temperature since, below 800 °C, soot is oxidized only to CO₂, but above 800 °C, CO is the main product of soot oxidation. Therefore, depending on the presence or absence of oxygen, the copper improved or worsened the catalytic performance.

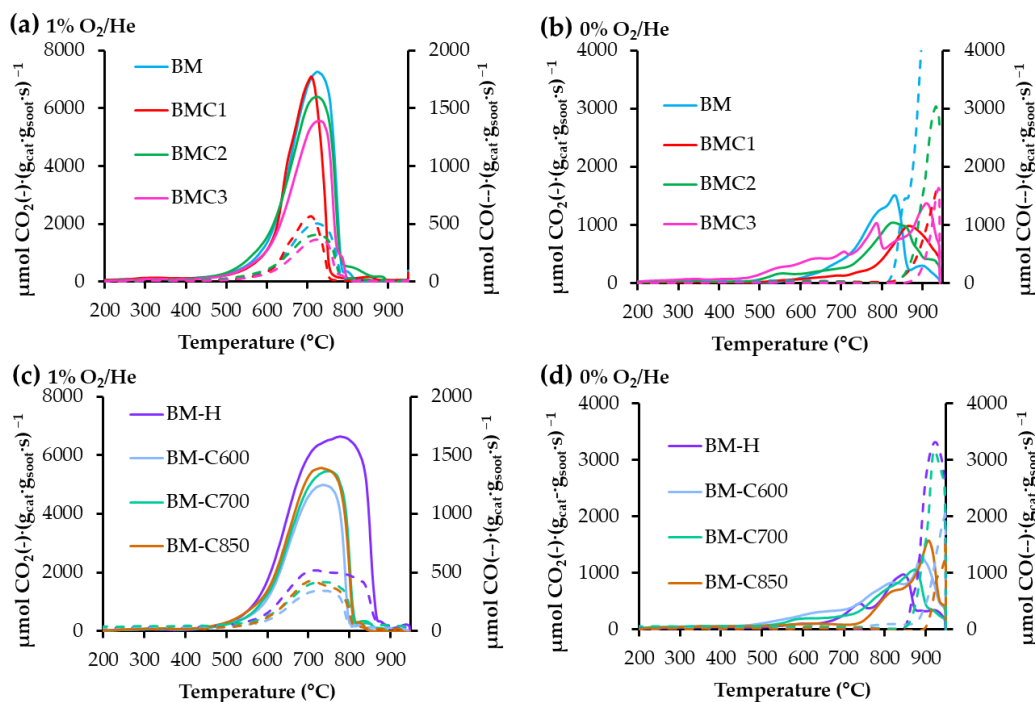


Figure 6. Evolved CO₂ (solid line) and CO (dotted line) profiles during soot oxidation: (a,c) in (1% O₂/He) and (b,d) in He.

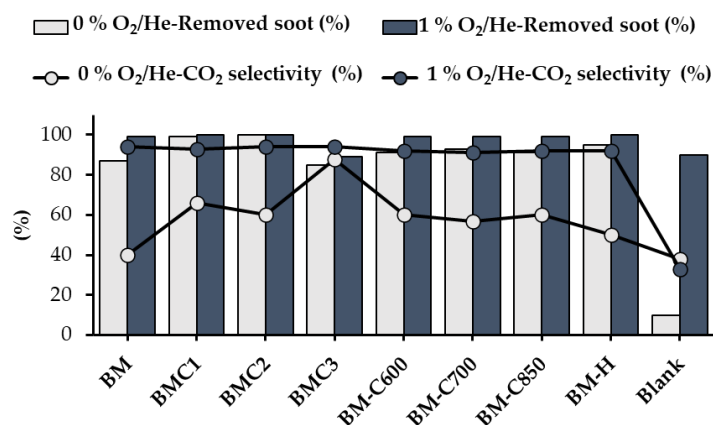


Figure 7. Percentage of removed soot and CO₂ selectivity values in He and 1% O₂/He for BaMn_{1-x}Cu_xO₃ and BaMnO₃ catalyst series.

The effect of the synthesis method is shown by the CO and CO₂ profiles presented in Figure 6c,d. As for the copper-containing catalysts, in the absence of oxygen, the catalysts were active at temperatures higher than 700 °C, because it is the temperature at which the β-O₂ is released (as observed in the O₂-TPD profiles in Figure 5). Note that the BaMnO₃ catalysts obtained through the hydrothermal and modified sol-gel methods presented a similar catalytic performance than BM; so, the synthesis method seems to not

significantly affect the catalytic activity. A similar conclusion has also been reported for $\text{La}_{0.9}\text{M}_{0.1}\text{MnO}_3$ [40] and $\text{La}_{0.6}\text{Sr}_{0.4}\text{MnO}_3$ [44].

The results show that only in the presence of catalysts was the oxidation carried out, but the synthesis method was not relevant since all the catalysts were able to remove almost 90% of the soot and they showed similar CO_2 selectivity (around 50%) at the end of the experiment.

On the contrary, the CO and CO_2 profiles under a 1% O_2/He atmosphere (Figure 6a,c) reveal that the catalytic activity was largely improved since the soot oxidation started at ca. 400 °C with the maximum being located at ca. 700 °C, while in inert atmosphere, the soot oxidation started at ca. 600 °C and the maximum was achieved at ca. 850 °C. Indeed, a similar catalytic performance was reported for other manganese-based perovskites, such as $\text{La}_{0.6}\text{Sr}_{0.4}\text{MnO}_3$ [72], $\text{La}_{1-x-y}\text{Sr}_x\text{Ag}_y\text{MnO}_3$ [69], SrMnO_3 and $\text{SrMn}_{0.98}(\text{Co,Cu})_{0.02}\text{O}_3$ [73]. This catalytic performance was attributed to the high capacity of manganese to activate oxygen, which was adsorbed in oxygen vacancies and then dissociated by the reduction of Mn (IV) to Mn (III) between 400 and 500 °C. Additionally, above 500 °C, the soot oxidation could also be performed by $\beta\text{-O}_2$ coming from the perovskite lattice. As the catalyzed soot oxidation is carried out at lower temperatures in the presence of 1% O_2/He , the soot oxidation to CO_2 is thermodynamically favored, according to the Ellingham diagram, so, as shown in Figure 7, higher CO_2 selectivity values were achieved.

In the absence of oxygen (He), as for the $\text{BaMn}_{1-x}\text{Cu}_x\text{O}_3$ series, the effect of the synthesis method or calcination temperature was not observed, and the only modification over the reaction was an increase in the selectivity to CO_2 .

To summarize, the catalysts were slightly active to oxidize soot under the highest demanding GDI conditions, i.e., in the absence of oxygen, but they presented a noticeably high CO_2 selectivity. The catalyst with the highest amount of copper (BMC3) showed the lowest percentage of soot removed but presented the highest CO_2 selectivity as it evolved the highest amount of $\beta\text{-O}_2$ of the series. For the BaMnO_3 catalysts, the highest activity was observed for BM-H, also because of the high amount of available oxygen ($\beta\text{-O}_2$), but no effect of the calcination temperature for the BM-CX samples was observed.

2.2.2. Second Phase: GC Experimental System

The study for soot oxidation in GDI conditions has been also analyzed using a GC, which allows the use of higher amounts of soot and a higher flow, these conditions being closer to the real application. Considering the results obtained in the preliminary study: (i) BMC2 was not included as BMC2 and BMC1 show the same catalytic behavior; and (ii) BM-C700 was used as the representative sample of the BM-CX series since no significant effect of the calcination temperature was observed.

The soot conversion, CO, and CO_2 emission profiles during the soot oxidation tests in He and 1% O_2/He atmospheres are shown in Figures 8 and 9, respectively. The temperature required to achieve 10% soot conversion (T10%) and the CO_2 selectivity values are gathered in Figure 10 in order to compare the activity data in both reaction atmospheres. Note that, in Figure 8a, 50% soot conversion was not achieved in the absence of oxygen; then, the T10% was compared instead of T50%. Figure 8a shows the soot conversion profiles under inert atmosphere, revealing that all catalysts were active since the soot oxidation was not carried out in the absence of the catalyst (blank). However, no effect of the amount of copper or the synthesis method was observed because all the BaMnO_3 catalysts removed over the 40% of the initial soot at the end of the test, showing a low CO_2 selectivity, which is the opposite trend observed in TG-MS conditions (Figure 7). This fact is a consequence of the different soot: catalyst ratio used (1:4 for GC and 1:8 for TG-MS) because, under inert atmosphere, oxygen is only supplied by the perovskite ($\beta\text{-O}_2$) [40,42,44,69,73]. Thus, once the perovskite is not able to supply oxygen, the passive oxidation of soot is performed, yielding CO as the main product, as is observed in Figure 9a.

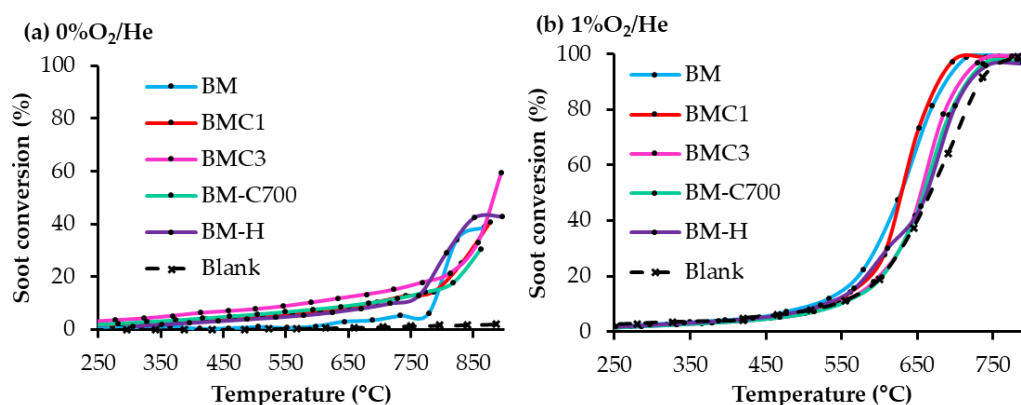


Figure 8. Soot conversion profiles in TPR conditions in (a) He and (b) 1% O₂/He for BaMnO₃ catalyst series.

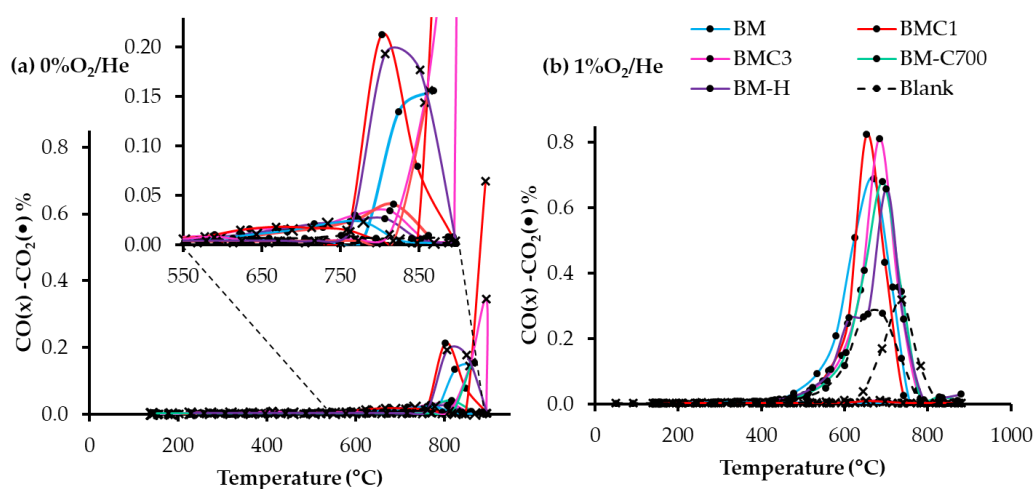


Figure 9. CO (x) and CO₂ (•) emission profiles in TPR conditions: (a) in He and (b) in 1% O₂/He for BaMnO₃ catalysts.

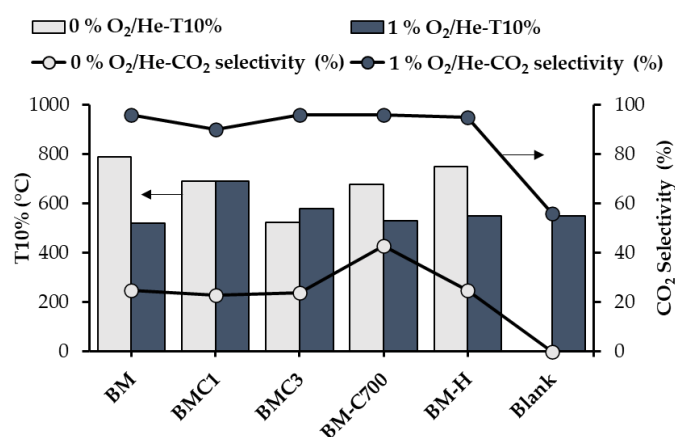


Figure 10. Temperature to achieve 10% soot conversion (T10%) and CO₂ selectivity values in He and 1% O₂/He for BaMnO₃ catalysts.

On the contrary, in the presence of 1% O₂/He, the catalyzed and uncatalyzed (blank) soot oxidation achieved 100% soot conversion (see Figure 10), but, in the presence of catalysts, the CO₂ selectivity significantly increased (reaching almost 100%), as has also been observed in TG-MS conditions. Therefore, BaMnO₃ catalysts are able to adsorb/activate oxygen from the reaction atmosphere and then transport it to the soot due to their high

oxygen mobility, as was proposed for perovskite-based catalysts [44] and for other metal-oxide-based catalysts [74]. Finally, an effect of the synthesis method (BM, BM-C700 and BM-H) or the copper amount (BMC1 and BMC3) was not observed since all the BaMnO₃ catalysts showed a similar T10%, which was close to that of the blank, and all the BaMnO₃-based catalysts showed a high CO₂ selectivity.

In summary, all the BaMnO₃ samples tested seemed to be active for the soot oxidation in the regular operation conditions for GDI engines [41], i.e., in the absence of oxygen, due to their capacity to supply oxygen coming from the perovskite lattice. However, a revealing effect of the synthesis method was not observed.

3. Materials and Methods

Materials: chemicals used as precursors: Citric acid (C₆H₈O₇ > 99.0%, Sigma Aldrich, St. Louis, MO, USA); ammonia (NH₃ 30%, Panreac, Darmstadt, Germany); barium acetate (Ba(C₂H₄O₂)₂ > 99.0%, Sigma Aldrich, St. Louis, MO, USA); magnesium (II) nitrate tetrahydrated (Mn(NO₃)₂·4H₂O > 99.0%, Sigma Aldrich, St. Louis, MO, USA); copper (II) nitrate trihydrated (Cu(NO₃)₂·3H₂O > 99.0%, Panreac, Darmstadt, Germany); carbon black (Vulcan XC-72R, CABOT, Boston, MS, USA); and model soot (PRINTEX-U, DEGUSA, Madrid, Spain).

3.1. Synthesis of Catalysts

3.1.1. Conventional Sol-Gel Method for the Synthesis of BaMn_{1-x}Cu_xO₃ Series [45]

For the conventional sol-gel synthesis of BaMnO₃(BM) and BaMn_{1-x}Cu_xO₃ (BMC3), barium, manganese and copper (for BMC3) precursors were added to a solution of citric acid (1M) with a pH of 8.5 (basified with ammonia solution); then, the solution was heated up to 65 °C for 5 h to obtain a gel, which was dried at 90 °C for 48 h, and finally was calcined at 150 °C (1 °C/min) for 1 h and at 850 °C (5 °C/min) for 6 h.

3.1.2. Modified Sol-Gel Method for The Synthesis of BM-CX Series [46]

The modified sol-gel method followed the above-mentioned steps but, after adding the precursors, carbon black was incorporated into the solution, with a mass ratio 1:1 regarding the mass of BaMnO₃, and vigorously stirred for 1 h. Then, the mixture was dried at 90 °C for 48 h, calcined at 150 °C (1 °C/min) for 1 h, and finally, at 600 °C, 700 °C or 850 °C (5 °C/min) for 6 h, to obtain BM-C600, BM-C700, and BM-C850.

3.1.3. Hydrothermal Method for The Synthesis of BM-H

For the hydrothermal synthesis of BM-H, the barium precursor was solved in deionized water at 90 °C for 1 h. Then, manganese precursors were added. After 15 min under magnetic stirring, the mixture was transferred to a stainless-steel autoclave and heated up to 90 °C for 72 h. The obtained solid was filtered, washed with deionized water, dried overnight at 90 °C, and calcined at 600 °C (5 °C/min) for 6 h.

3.2. Characterization Techniques

ICP-OES (Perkin-Elmer device model Optimal 4300 DV, Waltham, MA, USA) was used to measure the amount of copper on the copper-containing samples. The samples were mineralized by using a diluted aqua regia solution (HNO₃:HCl, 1:3) and stirring at room temperature for 1 h.

N₂ adsorption at −196 °C was achieved in an Autosorb-6B instrument from Quantachrome (Anton Paar Austria GmbH, Graz, Austria) to determine the textural properties. The samples were degassed at 250 °C for 4 h before the N₂ adsorption experiments.

The X-ray patterns were recorded between 20 and 80° 2θ angles with a step rate of 0.4°/min and using Cu Kα (0.15418 nm) radiation in a Bruker D8-Advance device (Billerica, MA, USA) in order to study the crystalline structure, and the average crystal size was determined by using the Scherrer equation, assuming k = 0.9.

The chemical surface properties were obtained through X-ray photoelectron spectroscopy (XPS), using a K-Alpha Photoelectron Spectrometer from Thermo-Scientific (Waltham, MA, USA) with an Al K α (1486.7 eV) radiation source. To obtain the XPS spectra, the pressure of the analysis chamber was maintained at 5×10^{-10} mbar. The binding energy (BE) and kinetic energy (KE) scales were adjusted by setting the C 1s transition at 284.6 eV, and the BE and KE values were then determined with the peak-fit software of the spectrometer. The XPS ratios $O_{\text{Lattice}}/(Ba + Mn)$, $Cu/(Ba + Mn + Cu)$ and $Mn(IV)/Mn(III)$ were calculated using the area under the suggested deconvolutions of O 1s, Mn 3p $^{3/2}$, Cu 2p $^{3/2}$ and Ba 3d $^{5/2}$ bands.

The reducibility of the catalysts was studied by temperature programmed reduction with H $_2$ (H $_2$ -TPR) in a Pulse Chemisorb 2705 (from Micromeritics, Norcross, GA, USA) with a thermal conductivity detector (TCD) and using 30 mg of sample, heated at 10 °C/min from 25 °C to 1000 °C in 5% H $_2$ /Ar atmosphere (40 mL/min). The quantification of the H $_2$ consumption was carried out using a CuO reference sample.

O $_2$ -TPD experiments were performed in a TG-MS (Q-600-TA and Thermostar from Balzers Instruments (Pfeiffer Vacuum GmbH, Asslar, Germany), respectively), with 16 mg of the sample heated at 5 °C/min from room temperature to 900 °C under a 100 mL/min of helium atmosphere. The 18, 28, 32 and 44 m/z signals were followed for H $_2$ O, CO, O $_2$ and CO $_2$, respectively, evolved during these experiments. The 40 m/z signal was also followed to ensure the tightness of the experimental system. The amount of evolved oxygen was estimated using a CuO reference sample.

3.3. Activity Test

The study of the soot oxidation in GDI conditions, in the absence (He) and very restrictive amounts of oxygen (1% O $_2$ /He), was developed in two phases to obtain complementary information. In both phases, the catalyst and the model soot were mixed with a spatula to ensure loose contact.

The preliminary phase was performed using the most favorable reaction conditions, i.e., low model soot:catalyst ratio (1:8) and a medium gas flow (100 mL/min). The experiments were carried out in a TG (Q-600-TA) coupled with a mass spectrometer (Omnistar-Vacuum Pfeiffer), to follow the m/z signals 18 (H $_2$ O), 28 (CO), 32 (O $_2$), and 44 (CO $_2$). To prove the tightness of the system, the m/z 40 (Ar) signal was also followed. Previously, the catalyst-soot mixture was dried at 150 °C for 1 h to remove the moisture, and then the temperature was raised from 150 °C to 900 °C (10 °C/min). The calibration was performed with calcium oxalate for 18 (H $_2$ O), 28 (CO), and 44 (CO $_2$) m/z signals, and copper oxide for a 32 (O $_2$) m/z signal.

The second phase was developed under conditions closer to the real application, and similar to those employed in the NO to NO $_2$ oxidation and diesel soot oxidation studies, that is, a higher ratio of model soot: catalyst (1:4) and a higher gas flow (500 mL/min). The reaction was carried out in a U-shaped quartz reactor, loaded with a diluted mixture of 80 mg of catalyst and 20 mg of model soot diluted in 300 mg SiC. The exit of the reactor was connected to a gas chromatograph (HP6890 series), equipped with two columns (Porapack-Q and MolSieve-13X) and a TCD. Before the experiment, the mixture was dried at 150 °C for 1 h to remove the moisture; then, the temperature was raised from 150 °C to 900 °C (5 °C/min).

The soot conversion and CO $_2$ selectivity were determined using Equations (1) and (2).

$$\text{Soot conversion (\%)} = \frac{\sum_0^t \text{CO}_2 + \text{CO}}{\sum_0^{\text{final}} (\text{CO}_2 + \text{CO})} \cdot 100 \quad (1)$$

$$\text{CO}_2 \text{ Selectivity (\%)} = \frac{\text{CO}_2}{\sum_0^{\text{final}} (\text{CO}_2 + \text{CO})} \cdot 100 \quad (2)$$

4. Conclusions

The conventional sol-gel, modified sol-gel, and hydrothermal synthesis methods were used to prepare BaMnO₃ perovskite-based solids. The characterization and activity results draw off the following conclusions:

- All synthesis methods allow the formation of BaMnO₃ solids with a perovskite-like structure, and only BMC3 presents the polytype structure as the majority phase due to the partial substitution of manganese by copper into the perovskite lattice.
- Mn (III) and Mn (IV) oxidation states coexist in all catalysts, with Mn (III) being the main oxidation state. The presence of copper causes an increase in the Mn (III) and in the amount of oxygen surface vacancies.
- Both strategies, the insertion of copper and using two different synthesis methods (hydrothermal and modified sol-gel synthesis), promote the formation of oxygen vacancies, the manganese reducibility and, hence, an improvement in the oxygen mobility.
- In the most favorable reaction conditions (preliminary study), a relationship was observed between the ability to catalyze the soot oxidation and the amount of β-O₂ evolved, showing that BM-H and BMC3 samples show the best performances under the hardest GDI scenarios. In the absence of oxygen in the reaction atmosphere, the oxygen supplied by the perovskite (i.e., the oxygen evolved during the O₂-TPD experiments) allows a high selectivity to CO₂, since the passive oxidation of soot is carried out and BaMnO₃ catalyzes the CO to CO₂ oxidation. In the presence of a low amount of oxygen (1% O₂ in He), the catalysts present a high activity to catalyze the CO to CO₂ oxidation.
- In the reactions carried out in more realistic conditions (second phase), all BaMnO₃-based catalysts, independently of the copper amount or the method used for synthesis, were active for soot oxidation in the absence of oxygen (He). In the presence of low amounts of oxygen (1% O₂/He), the catalysts present a high CO₂ selectivity.
- All BaMnO₃ samples tested seem to be active for the soot oxidation in the regular operation conditions for GDI engines [41], i.e., in the absence of oxygen, due to their capacity to supply oxygen coming from the perovskite lattice. However, a revealing effect of the synthesis method was not observed.

Author Contributions: Conceptualization, V.T.-R. and M.-J.I.-G.; methodology, V.T.-R.; validation, V.T.-R. and M.-J.I.-G.; formal analysis, V.T.-R., M.-S.S.-A. and M.-J.I.-G.; investigation, V.T.-R.; resources, V.T.-R., M.-S.S.-A. and M.-J.I.-G.; data curation, V.T.-R.; writing—original draft preparation, V.T.-R.; writing—review and editing, M.-J.I.-G.; visualization, M.-S.S.-A.; supervision M.-J.I.-G.; project administration M.-J.I.-G.; funding acquisition M.-J.I.-G. All authors have read and agreed to the published version of the manuscript.

Funding: This research was funded by Generalitat Valenciana (CIPROM/2021/70), Spanish Government (PID2019-105542RB-I00) and EU (FEDER Funding).

Data Availability Statement: Not applicable.

Conflicts of Interest: The authors declare no conflict of interest.

Appendix A

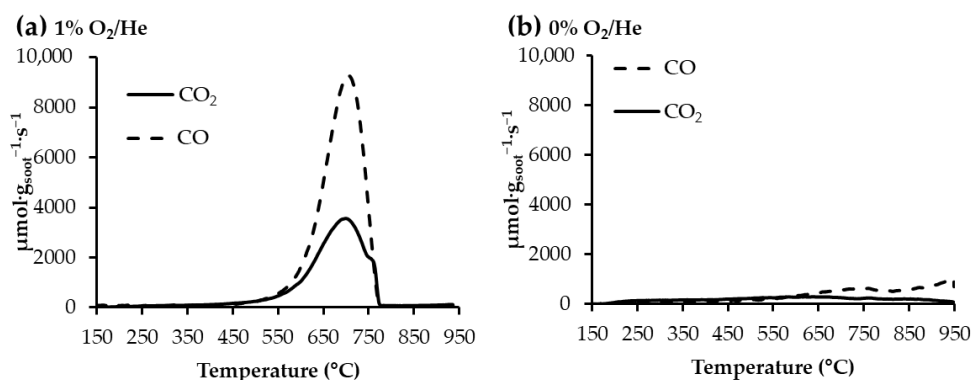


Figure A1. Evolved CO₂ and CO profiles for uncatalyzed soot oxidation: (a) in 1% O₂/He and (b) in He.

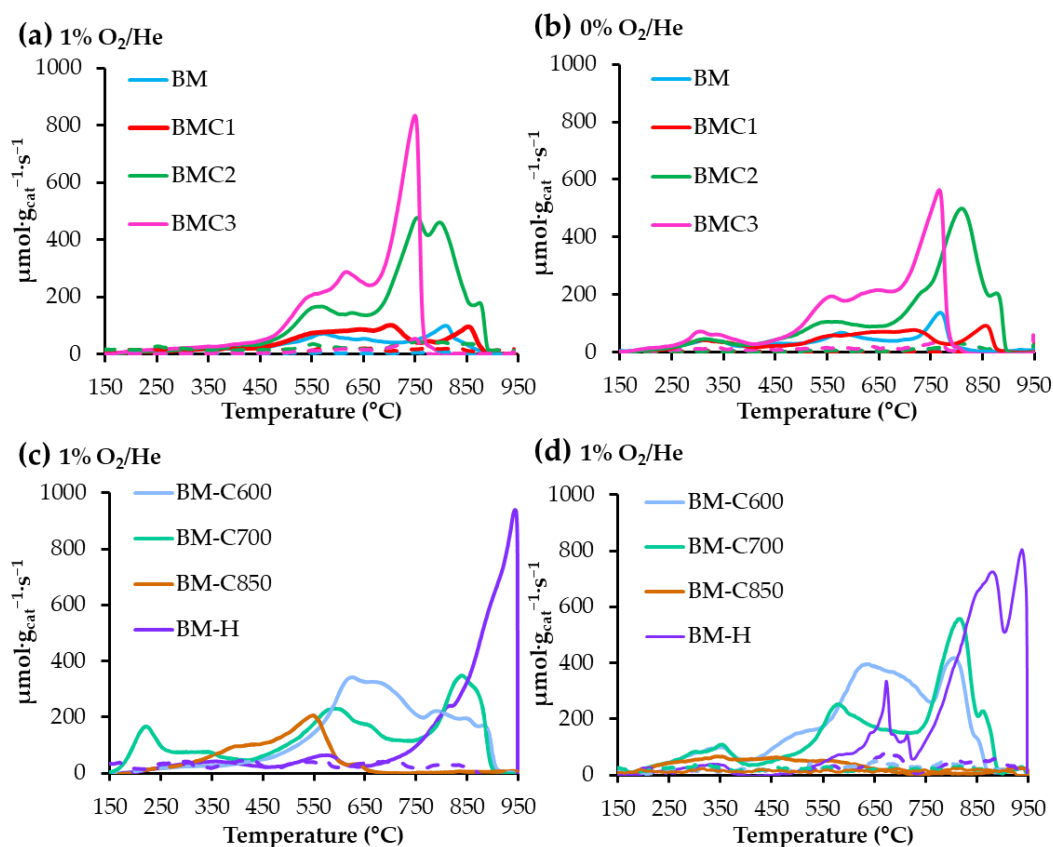


Figure A2. Evolved CO₂ and CO profiles for catalysts: (a,c) in (1% O₂/He) and (b,d) in He.

References

1. Pacella, M.; Garbujo, A.; Fabro, J.; Guiotto, M.; Xin, Q.; Natile, M.M.; Canu, P.; Cool, P.; Glisenti, A. PGM-Free CuO/LaCoO₃ Nanocomposites: New Opportunities for TWC Application. *Appl. Catal. B Environ.* **2018**, *227*, 446–458. [[CrossRef](#)]
2. Glisenti, A.; Pacella, M.; Guiotto, M.; Natile, M.M.M.; Canu, P. Largely Cu-Doped LaCo_{1-x}Cu_xO₃ Perovskites for TWC: Toward New PGM-Free Catalysts. *Appl. Catal. B Environ.* **2016**, *180*, 94–105. [[CrossRef](#)]
3. Wu, J.; Dacquin, J.P.; Cordier, C.; Dujardin, C.; Granger, P. Optimization of the Composition of Perovskite Type Materials for Further Elaboration of Four-Way Catalysts for Gasoline Engine. *Top. Catal.* **2019**, *62*, 368–375. [[CrossRef](#)]
4. Yi, Y.; Liu, H.; Chu, B.; Qin, Z.; Dong, L.; He, H.; Tang, C.; Fan, M.; Bin, L. Catalytic Removal NO by CO over LaNi_{0.5}M_{0.5}O₃ (M = Co, Mn, Cu) Perovskite Oxide Catalysts: Tune Surface Chemical Composition to Improve N₂ Selectivity. *Chem. Eng. J.* **2019**, *369*, 511–521. [[CrossRef](#)]

5. Wu, J.; Dacquain, J.P.; Djelal, N.; Cordier, C.; Dujardin, C.; Granger, P. Calcium and Copper Substitution in Stoichiometric and La-Deficient LaFeO₃ Compositions: A Starting Point in next Generation of Three-Way-Catalysts for Gasoline Engines. *Appl. Catal. B Environ.* **2021**, *282*, 119621. [[CrossRef](#)]
6. Pinto, D.; Glisenti, A. Pulsed Reactivity on LaCoO₃-Based Perovskites: A Comprehensive Approach to Elucidate the CO Oxidation Mechanism and the Effect of Dopants. *Catal. Sci. Technol.* **2019**, *9*, 2749–2757. [[CrossRef](#)]
7. De Zanet, A.; Peron, G.; Natile, M.M.; Vittadini, A.; Glisenti, A. Synthesis and Development of Four Way Catalysts Starting from Critical Raw Material Free Perovskites: Influence of Doping and Synthesis Conditions. *Top. Catal.* **2019**, *62*, 237–243. [[CrossRef](#)]
8. Bartel, C.J.; Sutton, C.; Goldsmith, B.R.; Ouyang, R.; Musgrave, C.B.; Ghiringhelli, L.M.; Scheffler, M. New Tolerance Factor to Predict the Stability of Perovskite Oxides and Halides. *Sci. Adv.* **2019**, *5*, eaav0693. [[CrossRef](#)] [[PubMed](#)]
9. Peña, M.A.; Fierro, J.L.G. Chemical Structures and Performance of Perovskite Oxides. *Chem. Rev.* **2001**, *101*, 1981–2017. [[CrossRef](#)] [[PubMed](#)]
10. Zhang, R.; Villanueva, A.; Alamdari, H.; Kaliaguine, S. Catalytic Reduction of NO by Propene over LaCo_{1-x}Cu_xO₃ Perovskites Synthesized by Reactive Grinding. *Appl. Catal. B Environ.* **2006**, *64*, 220–233. [[CrossRef](#)]
11. Yamazoe, N.; Teraoka, Y. Oxidation Catalysis of Perovskites-Relationship to Bulk Structure and Composition (Valency, Defect, etc.). *Catal. Today* **1990**, *8*, 175–199. [[CrossRef](#)]
12. Royer, S.; Duprez, D. Catalytic Oxidation of Carbon Monoxide over Transition Metal Oxides. *ChemCatChem* **2011**, *3*, 24–65. [[CrossRef](#)]
13. Huang, C.; Zhu, Y.; Wang, X.; Liu, X.; Wang, J.; Zhang, T. Sn Promoted BaFeO_{3-Δ} Catalysts for N₂O Decomposition: Optimization of Fe Active Centers. *J. Catal.* **2017**, *347*, 9–20. [[CrossRef](#)]
14. Giménez-Mañogil, J.; Bueno-López, A.; García-García, A. Preparation, Characterisation and Testing of CuO/Ce_{0.8}Zr_{0.2}O₂ Catalysts for NO Oxidation to NO₂ and Mild Temperature Diesel Soot Combustion. *Appl. Catal. B Environ.* **2014**, *152–153*, 99–107. [[CrossRef](#)]
15. Wang, L.; Fang, S.; Feng, N.; Wan, H.; Guan, G. Efficient Catalytic Removal of Diesel Soot over Mg Substituted K/La_{0.8}Ce_{0.2}CoO₃ Perovskites with Large Surface Areas. *Chem. Eng. J.* **2016**, *293*, 68–74. [[CrossRef](#)]
16. López-Suárez, F.E.; Bueno-López, A.; Illán-Gómez, M.J.; Trawczynski, J. Potassium-Copper Perovskite Catalysts for Mild Temperature Diesel Soot Combustion. *Appl. Catal. A Gen.* **2014**, *485*, 214–221. [[CrossRef](#)]
17. López-Suárez, F.E.; Parres-Esclapez, S.; Bueno-López, A.; Illán-Gómez, M.J.; Ura, B.; Trawczynski, J. Role of Surface and Lattice Copper Species in Copper-Containing (Mg/Sr)TiO₃ Perovskite Catalysts for Soot Combustion. *Appl. Catal. B Environ.* **2009**, *93*, 82–89. [[CrossRef](#)]
18. Onrubia-Calvo, J.A.; Pereda-Ayo, B.; De-La-Torre, U.; González-Velasco, J.R. Strontium Doping and Impregnation onto Alumina Improve the NO_x Storage and Reduction Capacity of LaCoO₃ Perovskites. *Catal. Today* **2019**, *333*, 208–218. [[CrossRef](#)]
19. Schwickardi, M.; Johann, T.; Schmidt, W.; Schüth, F. High-Surface-Area Oxides Obtained by an Activated Carbon Route. *Chem. Mater.* **2002**, *14*, 3913–3919. [[CrossRef](#)]
20. Gao, Y.; Wu, X.; Liu, S.; Weng, D.; Zhang, H.; Ran, R. Formation of BaMnO₃ in Ba/MnO_x-CeO₂ Catalyst upon the Hydrothermal Ageing and Its Effects on Oxide Sintering and Soot Oxidation Activity. *Catal. Today* **2015**, *253*, 83–88. [[CrossRef](#)]
21. Nguyen, S.V.; Szabo, V.; Trong On, D.; Kaliaguine, S. Mesoporous Silica Supported LaCoO₃ Perovskites as Catalysts for Methane Oxidation. *Microporous Mesoporous Mater.* **2002**, *54*, 51–61. [[CrossRef](#)]
22. Yan, X.; Huang, Q.; Li, B.; Xu, X.; Chen, Y.; Zhu, S.; Shen, S. Catalytic Performance of LaCo_{0.5}M_{0.5}O₃ (M=Mn, Cr, Fe, Ni, Cu) Perovskite-Type Oxides and LaCo_{0.5}Mn_{0.5}O₃ supported on Cordierite for CO Oxidation. *J. Ind. Eng. Chem.* **2013**, *19*, 561–565. [[CrossRef](#)]
23. Schneider, R.; Kießling, D.; Wendt, G. Cordierite Monolith Supported Perovskite-Type Oxides—Catalysts for the Total Oxidation of Chlorinated Hydrocarbons. *Appl. Catal. B Environ.* **2000**, *28*, 187–195. [[CrossRef](#)]
24. Hu, Y.; Wang, X.; Tan, M.; Zou, X.; Ding, W.; Lu, X. Perovskite LaNiO₃ Nanocrystals inside SBA-15 Silica: High Stability and Anti-Coking Performance in the Pre-Reforming of Liquefied Petroleum Gas at a Low Steam-to-Carbon Molar Ratio. *ChemCatChem* **2016**, *8*, 1055–1058. [[CrossRef](#)]
25. Wu, Y.; Chu, B.; Zhang, M.; Yi, Y.; Dong, L.; Fan, M.; Jin, G.; Zhang, L.; Li, B. Influence of Calcination Temperature on the Catalytic Properties of LaCu_{0.25}Co_{0.75}O₃ Catalysts in NO_x Reduction. *Appl. Surf. Sci.* **2019**, *481*, 1277–1286. [[CrossRef](#)]
26. Zhuang, S.; Liu, Y.; Zeng, S.; Lv, J.; Chen, X.; Zhang, J. A Modified Sol-Gel Method for Low-Temperature Synthesis of Homogeneous Nanoporous La_{1-x}Sr_xMnO₃ with Large Specific Surface Area. *J. Sol-Gel Sci. Technol.* **2016**, *77*, 109–118. [[CrossRef](#)]
27. Milt, V.G.; Ulla, M.A.; Miró, E.E. NO_x Trapping and Soot Combustion on BaCoO_{3-y} Perovskite: LRS and FTIR Characterization. *Appl. Catal. B Environ.* **2005**, *57*, 13–21. [[CrossRef](#)]
28. Zhu, H.; Zhang, P.; Dai, S. Recent Advances of Lanthanum-Based Perovskite Oxides for Catalysis. *ACS Catal.* **2015**, *5*, 6370–6385. [[CrossRef](#)]
29. Tanaka, H.; Misono, M. Advances in Designing Perovskite Catalysts. *Curr. Opin. Solid State Mater. Sci.* **2001**, *5*, 381–387. [[CrossRef](#)]
30. Gunasekaran, N.; Rajadurai, S.; Carberry, J.J.; Bakshi, N.; Alcock, C.B. Surface Characterization and Catalytic Properties of La_{1-x}A_xMO₃ Perovskite Type Oxides. Part I. Studies on La_{0.95}Ba_{0.05}MO₃ (M = Mn, Fe or Co) Oxides. *Solid State Ionics* **1994**, *73*, 289–295. [[CrossRef](#)]
31. Rojas, M.L.; Fierro, J.L.G.; Tejuca, L.G.; Bell, T.A. Preparation and Characterization of LaMn_{1-x}Cu_xO_{3+Δ}; Perovskite Oxides. *J. Catal.* **1990**, *124*, 41–51. [[CrossRef](#)]

32. Royer, S.; Bérubé, F.; Kaliaguine, S. Effect of the Synthesis Conditions on the Redox and Catalytic Properties in Oxidation Reactions of LaCo_{1-x}Fe_xO₃. *Appl. Catal. A Gen.* **2005**, *282*, 273–284. [[CrossRef](#)]
33. Roy, C.; Budhani, R.C. Raman, Infrared and X-Ray Diffraction Study of Phase Stability in La_{1-x}Ba_xMnO₃ Doped Manganites. *J. Appl. Phys.* **1999**, *85*, 3124–3131. [[CrossRef](#)]
34. Caignaert, V.; Hervieu, M.; Domenges, B.; Nguyen, N. BaMn_{1-x}Fe_xO_{3-γ}, An Oxygen-Deficient 6H' Oxide: Electron Microscopy, Powder Neutron Diffraction, and Mössbauer Study. *J. Solid State Chem.* **1988**, *73*, 107–117. [[CrossRef](#)]
35. Patcas, F.; Buciuman, F.C.; Zsako, J. Oxygen Non-Stoichiometry and Reducibility of B-Site Substituted Lanthanum Manganites. *Thermochim. Acta* **2000**, *360*, 71–76. [[CrossRef](#)]
36. Khaskheli, A.A.; Xu, L.; Liu, D. Manganese Oxide-Based Catalysts for Soot Oxidation: A Review on the Recent Advances and Future Directions. *Energy Fuels* **2022**, *36*, 7362–7381. [[CrossRef](#)]
37. Zhang, R.; Villanueva, A.; Alamdari, H.; Kaliaguine, S. SCR of NO by Propene over Nanoscale LaMn_{1-x}Cu_xO₃ Perovskites. *Appl. Catal. A Gen.* **2006**, *307*, 85–97. [[CrossRef](#)]
38. Dhakad, M.; Rayalu, S.S.; Kumar, R.; Doggali, P.; Bakardjieva, S.; Subrt, J.; Mitsushashi, T.; Haneda, H.; Labhsetwar, N. Low Cost, Ceria Promoted Perovskite Type Catalysts for Diesel Soot Oxidation. *Catal. Lett.* **2008**, *121*, 137–143. [[CrossRef](#)]
39. Shangguan, W.F.F.; Teraoka, Y.; Kagawa, S. Kinetics of Soot-O₂, Soot-NO and Soot-O₂-NO Reactions over Spinel-Type CuFe₂O₄ Catalyst. *Appl. Catal. B Environ.* **1997**, *12*, 237–247. [[CrossRef](#)]
40. Zhao, H.; Sun, L.; Fu, M.; Mao, L.; Zhao, X.; Zhang, X.; Xiao, Y.; Dong, G. Effect of A-Site Substitution on the Simultaneous Catalytic Removal of NO_x and Soot by LaMnO₃ Perovskites. *New J. Chem.* **2019**, *43*, 11684–11691. [[CrossRef](#)]
41. Boger, T.; Rose, D.; Nicolin, P.; Gunasekaran, N.; Glasson, T. Oxidation of Soot (Printex[®]U) in Particulate Filters Operated on Gasoline Engines. *Emiss. Control Sci. Technol.* **2015**, *1*, 49–63. [[CrossRef](#)]
42. Martinovic, F.; Galletti, C.; Bensaid, S.; Pirone, R.; Deorsola, F.A. Soot Oxidation in Low-O₂ and O₂-Free Environments by Lanthanum-Based Perovskites: Structural Changes and the Effect of Ag Doping. *Catal. Sci. Technol.* **2022**, *12*, 5453–5464. [[CrossRef](#)]
43. Matarrese, R. Catalytic Materials for Gasoline Particulate Filters Soot Oxidation. *Catalysts* **2021**, *11*, 890. [[CrossRef](#)]
44. Hernández, W.Y.Y.; Tsampas, M.N.N.; Zhao, C.; Boreave, A.; Bosselet, F.; Vernoux, P. La/Sr-Based Perovskites as Soot Oxidation Catalysts for Gasoline Particulate Filters. *Catal. Today* **2015**, *258*, 525–534. [[CrossRef](#)]
45. Torregrosa-Rivero, V.; Albaladejo-Fuentes, V.; Sánchez-Adsuar, M.-S.S.; Illán-Gómez, M.-J.J. Copper Doped BaMnO₃ Perovskite Catalysts for NO Oxidation and NO₂-Assisted Diesel Soot Removal. *RSC Adv.* **2017**, *7*, 35228–35238. [[CrossRef](#)]
46. Torregrosa-Rivero, V.; Sánchez-Adsuar, M.S.; Illán-Gómez, M.J. Improving the Performance of BaMnO₃ Perovskite as Soot Oxidation Catalyst Using Carbon Black during Sol-Gel Synthesis. *Nanomaterials* **2022**, *12*, 219. [[CrossRef](#)]
47. Torregrosa-Rivero, V.; Sánchez-Adsuar, M.S.; Illán-Gómez, M.J. Analyzing the Role of Copper in the Soot Oxidation Performance of BaMnO₃-Perovskite-Based Catalyst Obtained by Modified Sol-Gel Synthesis. *Fuel* **2022**, *328*, 125258. [[CrossRef](#)]
48. Royer, S.; Duprez, D.; Can, F.; Courtois, X.; Batiot-Dupeyrat, C.; Laassiri, S.; Alamdari, H. Perovskites as Substitutes of Noble Metals for Heterogeneous Catalysis: Dream or Reality. *Chem. Rev.* **2014**, *114*, 10292–10368. [[CrossRef](#)]
49. Yang, Q.; Liu, G.; Liu, Y. Perovskite-Type Oxides as the Catalyst Precursors for Preparing Supported Metallic Nanocatalysts: A Review. *Ind. Eng. Chem. Res.* **2018**, *57*, 1–17. [[CrossRef](#)]
50. Kim, C.H.; Qi, G.; Dahlberg, K.; Li, W. Strontium-Doped Perovskites Rival Platinum Catalysts for Treating NO_x in Simulated Diesel Exhaust. *Science* **2010**, *327*, 1624–1627. [[CrossRef](#)]
51. Chen, J.; Shen, M.; Wang, X.; Qi, G.; Wang, J.; Li, W. The Influence of Nonstoichiometry on LaMnO₃ Perovskite for Catalytic NO Oxidation. *Appl. Catal. B Environ.* **2013**, *134–135*, 251–257. [[CrossRef](#)]
52. Niu, J.; Deng, J.; Liu, W.; Zhang, L.; Wang, G.; Dai, H.; He, H.; Zi, X. Nanosized Perovskite-Type Oxides La_{1-x}Sr_xMO_{3-δ} (M = Co, Mn; x = 0, 0.4) for the Catalytic Removal of Ethylacetate. *Catal. Today* **2007**, *126*, 420–429. [[CrossRef](#)]
53. Di Castro, V.; Polzonetti, G. XPS Study of MnO Oxidation. *J. Electron Spectros. Relat. Phenomena* **1989**, *48*, 117–123. [[CrossRef](#)]
54. Afzal, S.; Quan, X.; Zhang, J. High Surface Area Mesoporous Nanocast LaMO₃ (M = Mn, Fe) Perovskites for Efficient Catalytic Ozonation and an Insight into Probable Catalytic Mechanism. *Appl. Catal. B Environ.* **2017**, *206*, 692–703. [[CrossRef](#)]
55. Najjar, H.; Lamonier, J.F.; Mentré, O.; Giraudon, J.M.; Batis, H. Optimization of the Combustion Synthesis towards Efficient LaMnO_{3+y} Catalysts in Methane Oxidation. *Appl. Catal. B Environ.* **2011**, *106*, 149–159. [[CrossRef](#)]
56. Najjar, H.; Batis, H. La-Mn Perovskite-Type Oxide Prepared by Combustion Method: Catalytic Activity in Ethanol Oxidation. *Appl. Catal. A Gen.* **2010**, *383*, 192–201. [[CrossRef](#)]
57. Zhang, C.; Wang, C.; Hua, W.; Guo, Y.; Lu, G.; Gil, S.; Giroir-Fendler, A. Relationship between Catalytic Deactivation and Physicochemical Properties of LaMnO₃ Perovskite Catalyst during Catalytic Oxidation of Vinyl Chloride. *Appl. Catal. B Environ.* **2016**, *186*, 173–183. [[CrossRef](#)]
58. Merino, N.A.; Barbero, B.P.; Eloy, P.; Cadús, L.E. La_{1-x}Ca_xCoO₃ Perovskite-Type Oxides: Identification of the Surface Oxygen Species by XPS. *Appl. Surf. Sci.* **2006**, *253*, 1489–1493. [[CrossRef](#)]
59. Albaladejo-Fuentes, V.; López-Suárez, F.E.; Sánchez-Adsuar, M.S.; Illán-Gómez, M.J. Tailoring the Properties of BaTi_{0.8}Cu_{0.2}O₃ Catalyst Selecting the Synthesis Method. *Appl. Catal. A Gen.* **2016**, *519*, 7–15. [[CrossRef](#)]
60. Albaladejo-Fuentes, V.; López-Suárez, F.E.; Sánchez-Adsuar, M.S.; Illán-Gómez, M.J. BaTi_{1-x}Cu_xO₃ Perovskites: The Effect of Copper Content in the Properties and in the NO_x Storage Capacity. *Appl. Catal. A Gen.* **2014**, *488*, 189–199. [[CrossRef](#)]

61. Bnciuman, F.C.; Patcas, F.; Zsakó, J. TPR-Study of Substitution Effects on Reducibility and Oxidative Non-Stoichiometry of $\text{La}_{0.8}\text{A}'_{0.2}\text{MnO}_{3+\delta}$ Perovskites. *J. Therm. Anal. Calorim.* **2000**, *61*, 819–825. [[CrossRef](#)]
62. Irusta, S.; Pina, M.P.; Menéndez, M.; Santamaría, J. Catalytic Combustion of Volatile Organic Compounds over La-Based Perovskites. *J. Catal.* **1998**, *179*, 400–412. [[CrossRef](#)]
63. Irusta, S.; Pina, M.P.; Menéndez, M.; Santamaría, J. Development and Application of Perovskite-Based Catalytic Membrane Reactors. *Catal. Lett.* **1998**, *54*, 69–78. [[CrossRef](#)]
64. Peron, G.; Glisenti, A. Perovskites as Alternatives to Noble Metals in Automotive Exhaust Abatement: Activation of Oxygen on LaCrO_3 and LaMnO_3 . *Top. Catal.* **2019**, *62*, 244–251. [[CrossRef](#)]
65. Tien-Thao, N.; Alamdari, H.; Zahedi-Niaki, M.H.H.; Kaliaguine, S. $\text{LaCo}_{1-x}\text{Cu}_x\text{O}_{3-\delta}$ Perovskite Catalysts for Higher Alcohol Synthesis. *Appl. Catal. A Gen.* **2006**, *311*, 204–212. [[CrossRef](#)]
66. Levasseur, B.; Kaliaguine, S. Effect of the Rare Earth in the Perovskite-Type Mixed Oxides AMnO_3 (A = Y, La, Pr, Sm, Dy) as Catalysts in Methanol Oxidation. *J. Solid State Chem.* **2008**, *181*, 2953–2963. [[CrossRef](#)]
67. Najjar, H.; Batis, H. Development of Mn-Based Perovskite Materials: Chemical Structure and Applications. *Catal. Rev.* **2016**, *58*, 371–438. [[CrossRef](#)]
68. Kalogirou, M.; Samaras, Z. A Thermogravimetric Kinetic Study of Uncatalyzed Diesel Soot Oxidation. *J. Therm. Anal. Calorim.* **2009**, *98*, 215–224. [[CrossRef](#)]
69. Hernández, W.Y.; Lopez-Gonzalez, D.; Ntais, S.; Zhao, C.; Boréave, A.; Vernoux, P. Silver-Modified Manganite and Ferrite Perovskites for Catalyzed Gasoline Particulate Filters. *Appl. Catal. B Environ.* **2018**, *226*, 202–212. [[CrossRef](#)]
70. Torregrosa-Rivero, V.; Moreno-Marcos, C.; Albaladejo-Fuentes, V.; Sánchez-Adsuar, M.S.; Illán-Gómez, M.J. $\text{BaFe}_{1-x}\text{Cu}_x\text{O}_3$ Perovskites as Active Phase for Diesel (DPF) and Gasoline Particle Filters (GPF). *Nanomaterials* **2019**, *9*, 1551. [[CrossRef](#)]
71. Moreno-Marcos, C.; Torregrosa-Rivero, V.; Albaladejo-Fuentes, V.; Sánchez-Adsuar, M.S.; Illán-Gómez, M.J. $\text{BaFe}_{1-x}\text{Cu}_x\text{O}_3$ Perovskites as Soot Oxidation Catalysts for Gasoline Particulate Filters (GPF): A Preliminary Study. *Top. Catal.* **2019**, *62*, 413–418. [[CrossRef](#)]
72. Arandiyán, H.; Dai, H.; Deng, J.; Liu, Y.; Bai, B.; Wang, Y.; Li, X.; Xie, S.; Li, J. Three-Dimensionally Ordered Macroporous $\text{La}_{0.6}\text{Sr}_{0.4}\text{MnO}_3$ with High Surface Areas: Active Catalysts for the Combustion of Methane. *J. Catal.* **2013**, *307*, 327–339. [[CrossRef](#)]
73. Uppara, H.P.; Pasupathy, J.S.; Pradhan, S.; Singh, S.K.; Labhsetwar, N.K.; Dasari, H. The Comparative Experimental Investigations of $\text{SrMn}(\text{Co}^{3+}/\text{Co}^{2+})\text{O}_{3\pm\delta}$ and $\text{SrMn}(\text{Cu}^{2+})\text{O}_{3\pm\delta}$ Perovskites towards Soot Oxidation Activity. *Mol. Catal.* **2020**, *482*, 110665. [[CrossRef](#)]
74. Gross, M.S.; Ulla, M.A.; Querini, C.A. Diesel Particulate Matter Combustion with CeO_2 as Catalyst. Part I: System Characterization and Reaction Mechanism. *J. Mol. Catal. A Chem.* **2012**, *352*, 86–94. [[CrossRef](#)]